RESEARCH ARTICLE
ATMOSPHERIC PHYSICS

Earth and Planetary Physics
10: 482–496, 2026
doi: 10.26464/epp2026040

Multiscale energy conversion and transfer in the middle atmosphere during the 2023 sudden stratospheric warming

XiaoQi Wu[1,2], CunYing Xiao[1,2*], ZeWei Wang[1,2], Yang Yu[1,2], Luo Xiao[1,2], and Hao Li[1,2]

[1]Institute for Frontiers in Astronomy and Astrophysics, Beijing Normal University, Beijing 102206, China;

[2]School of Physics and Astronomy, Beijing Normal University, Beijing 100875, China

Key Points:

- Pressure flux played a critical role in coupling the mesosphere and stratosphere during the 2023 sudden stratospheric warming (SSW), facilitating vertical energy exchange between the two regions.
- Canonical transfer of available potential energy (APE) consistently flowed from the large-scale to the SSW-scale window in both the stratosphere and mesosphere, indicating that baroclinic instability is a dominant and robust mechanism across different SSW events.
- Compared with the 2012–2013 SSW, the 2023 event exhibited significantly stronger energy transfer magnitudes in the mesosphere, highlighting event-specific variability in mesospheric energetics.

Citation: Wu, X. Q., Xiao, C. Y., Wang, Z. W., Yu, Y., Xiao, L., and Li, H. (2026). Multiscale energy conversion and transfer in the middle atmosphere during the 2023 sudden stratospheric warming. *Earth Planet. Phys.*, *10*(3), 482–496. http://doi.org/10.26464/epp2026040

Abstract: To understand energy transfer during sudden stratospheric warming (SSW) events in the middle atmosphere, the 2023 SSW is studied by using the analysis tools of the multiscale window transform (MWT) and MWT-based localized energetics analysis and theory of canonical transfer (MS-ECT). The energy transfer in the mesosphere is diagnosed and compared with that in the stratosphere. The energy fields are first reconstructed onto three scale windows: a large-scale window, an SSW-scale window, and a synoptic-scale window. Results showed that the work done by pressure (pressure flux) plays a critical role in coupling the mesosphere and stratosphere during SSW events. The cross-scale energy transfer (canonical transfer) of available potential energy is always directed from the large-scale to the SSW-scale window, indicating the central role of baroclinic instability in both the stratosphere and mesosphere. Comparative analysis with the 2012–2013 SSW event revealed the consistent presence of baroclinic instability across both events. However, the 2023 event exhibited significantly stronger energy transfer magnitudes in the mesosphere. These results highlight the consistent role of baroclinic instability and pressure flux in mediating cross-scale energy transfer during SSWs, providing a clearer understanding of stratosphere–mesosphere coupling.

Keywords: sudden stratospheric warming; multiscale energetics analysis; middle atmosphere

1. Introduction

Energy conversion and transfer within the atmosphere are fundamental to the dynamics that govern climate variability and weather patterns. A key aspect of these dynamics is energy transfer within the atmosphere, which occurs through mechanisms such as radiation, convection, and wave propagation by means of energy conversion. This energy conversion and transfer is crucial for maintaining the atmospheric thermal structure and driving large-scale circulation patterns that affect weather systems, climate variability, and extreme weather events. In turn, these structures and processes also have an impact on the energy conversion and transfer within them. Sudden stratospheric warmings (SSWs) are particularly significant events in this context.

First author: X. Q. Wu, 202431101097@mail.bnu.edu.cn
Correspondence to: C. Y. Xiao, xiaocunying@bnu.edu.cn
Received 13 NOV 2025; Accepted 02 MAR 2026.
First Published online 24 MAR 2026.

An SSW is a kind of event involving a large and rapid temperature increase and sometimes a reversal of the zonal wind in the high-latitude region of the stratosphere (Scherhag, 1952). These events can have far-reaching effects, affecting not only changes in atmospheric circulation in the stratosphere, but also the winter troposphere and even the mesosphere. Sudden stratospheric warmings greatly affect the structural characteristics of and variations in the winter stratosphere as well as the entire atmospheric circulation. Since the discovery of SSWs, meteorological researchers have conducted extensive observations and research on them. Sudden stratospheric warmings are believed to be due to the interaction of upward-propagating planetary waves with zonal winds (Wüst and Bittner, 2011). Several phenomena related to the ocean–atmosphere system, such as the El Niño–Southern Oscillation (ENSO) and Madden–Julian Oscillation (MJO) outside the polar stratosphere, have been identified as possible modulators of the likelihood of SSWs (Baldwin et al., 2021). Roy and Kuttippurath (2022) studied the dynamic evolution and activities of waves in SSWs of arctic winters over the decade of 2011–2021. Many studies

have been conducted on the impact of SSWs on stratospheric atmospheric fluctuations (Kalisch and Chun, 2021; Mitra et al., 2022). Recently, many studies have paid attention to variations in SSWs in the mesosphere and lower thermosphere (MLT) region. Long-term studies, such as that by Li QR et al. (2024), have shown that variations in planetary wave activity are a primary driver of arctic SSW frequency and characteristics, underscoring the critical role of wave–mean flow interactions. Some have studied atmospheric variations in the MLT regions during SSW periods. In particular, ground-based meteor radars, such as those deployed in the Chinese Meridian Project, have provided continuous and stable wind observations in the MLT region, greatly advancing our understanding of planetary wave behaviors during SSWs (Ma Z et al., 2024). Sudden stratospheric warmings have been found to be closely related to the cooling of the mesosphere and the warming of the lower part of the thermosphere (Chen X et al., 2012; Zorkaltseva et al., 2019; Kohma et al., 2021). For instance, Yang JF et al. (2024) reported a rapid increase of more than 50% in high-latitude mesospheric neutral air density around the onset of the major 2021 SSW, which they attributed to altered planetary waves and residual circulation. Energy deposition and redistribution during upper atmospheric disturbances often exhibit complex spatial patterns. In the mesosphere, gravity waves often play a more dominant role during SSW events, whereas modulations of gravity wave activity and wave forcing in the mesosphere have been observed, and these play a critical role in the recovery of the westward zonal-mean zonal winds in the mesosphere after the SSW event (Tomikawa et al., 2012). Recent observations using COSMIC (Constellation Observing System for Meteorology, Ionosphere, and Climate) data have also revealed enhanced gravity wave potential energy density during SSWs, with eastward and downward extensions and a strong relationship with zonal wind weakening (Zeng XY and Zhong G, 2024). However, existing research still lacks quantitative contributions to the energy transfer between the lower stratosphere and upper mesosphere during SSWs, which is also particularly valuable, as it would reveal the mechanisms behind these sudden temperature and wind changes and would provide important insights into mesosphere–stratosphere coupling. Such research would help explain the transmissions between different energy sources in the atmosphere. The physical mechanisms by which SSWs have an impact on the mesosphere are not well understood, and answering this question would extend scientific curiosity in a society extremely dependent on technology affected by space weather (Baldwin et al., 2021).

The atmospheric energy cycle is a useful tool for diagnosing atmospheric circulation because it can reflect the physical mechanisms of multilevel interactions and transformations in the climate system. The energetic transfer diagnostics in the atmosphere during SSWs are important for understanding the influences of SSWs on the entire atmospheric circulation. The Lorenz energy cycle diagnostic, introduced by Lorenz (1955), has proved to be particularly useful in analyzing atmospheric energetics. Over the years, various multiscale energetics analyses have been conducted on the energetics averaged over a specific domain (e.g., Julian and Labitzke, 1965; Trenberth, 1973). However, these analyses do not distinguish between different spatial locations, which limits their ability to capture regional variations. This information is especially relevant for SSW events, which are transient events that occur over a short period each year, marked by a rapid temperature increase within just a few days. Because these events are nonstationary, the time–mean decomposition method fails to effectively separate such short-term, dynamic processes. Beyond externally driven formation processes, emerging studies propose that SSWs may originate from intrinsic atmospheric dynamics. In foundational work, Plumb (1981) theorized that temporal growth in these events could stem from resonant interactions between stationary planetary waves and decelerating progressive waves. His analysis further distinguished between displacement-type SSWs (characterized by polar vortex shifting) and split-type SSWs (featuring vortex fragmentation), positing fundamentally distinct generation pathways for these phenomena. To unravel the atmospheric system's preferential selection of specific formation mechanisms, comprehensive energy budget analyses can serve as crucial investigative tools, particularly for differentiating between competing dynamic processes. Liang XS (2016) found the multiscale window transform (MWT) of Liang XS and Anderson (2007) to be a powerful method of overcoming the difficulties mentioned above. This discovery has also led to a new diagnostic methodology, that is, the localized energetics analysis and theory of canonical transfer (MS-ECT). These two methods have been applied successfully to oceanic and atmospheric diagnoses (Yang Y, et al., 2017; Wei JN and Zhang J, 2021; Wang ML and Liang XS, 2022; Ma JW and Liang XS, 2023).

Xu F and Liang XS (2017) applied the MWT and the localized multiscale energy and vorticity analysis (MS-EVA) to diagnose the energetic transforms during a 2012–2013 SSW event in the stratosphere. They applied the multiscale method to their study, conducted some vorticity analyses, and used the theory of canonical transfer. From their study, we can conclude that in the stage of rapid warming, the temperature rise is mainly due to a strong poleward heat flux and a canonical transfer through baroclinic instability, which extracts the available potential energy (APE) from the mean window. At that time, a portion of the SSW-scale APE is converted to the SSW-scale kinetic energy (KE). However, how the energy transfer in the mesosphere occurs during SSW events is unknown. Open questions are whether it is similar to or opposite of the situation in the stratosphere, what influence it has, and whether different characteristics correspond to different SSW events.

With the aim of deeply understanding how the energy is transferred in the middle atmosphere, especially in the mesosphere, during SSWs and identifying whether the energy transfer characteristics are different between different SSW events, we use the MWT and MS-ECT to analyze the energy transfer at different scales during the 2023 SSW and the 2012–2013 SSW for comparisons based on Modern-Era Retrospective analysis for Research and Applications, Version 2 (MERRA-2) reanalysis data. This energetic diagnosis helps us understand more about the mechanisms of SSWs in the middle atmosphere. In addition, it contributes to understanding the relationship between different energy sources in the atmosphere, as well as the energy coupling and transmission

at different altitudes. Much of this variation in predictive skill is likely linked to limitations in the predictive skill of key tropospheric drivers of the SSW process (Baldwin et al., 2021). As noted by Noguchi et al. (2016), predictions of SSW events are also sensitive to the background stratospheric state prior to the SSW. Given the relevance of SSW events to the entire atmosphere, the predictability of SSWs can be improved by numerical simulation.

The data and the MWT and MS-ECT methods used are introduced in Section 2. The results are shown in Section 3. Sections 4 and 5 present the discussion and conclusions, respectively.

2. Data and Method

The data used in this study are the reanalysis product of MERRA-2 because of its high quality and availability at low altitudes. Along with the enhancements of MERRA-2 in meteorological assimilation, it takes significant steps toward the target of an earth system reanalysis set by the Global Modeling and Assimilation Office (GMAO) at the National Aeronautics and Space Administration (NASA). The MERRA-2 is the first long-term global reanalysis to assimilate space-based observations of aerosols and represent their interactions with other physical processes in the climate system (Gelaro et al., 2017). The data quality in the middle atmosphere improved after 2004 when the Earth Observing System (EOS) Aura satellite data were assimilated (Gelaro et al., 2017; Wargan et al., 2017). Many studies have used the MERRA-2 reanalysis database to investigate SSW events in the middle atmosphere. Koushik et al. (2020) used MERRA-2 data to study abrupt changes in stratopause winds during three SSW events. Eswaraiah et al. (2020) studied the mesosphere winds during a 2019 SSW using MERRA-2 data. Tang et al. (2023) used MERRA-2 data to analyze different quasi-2-day wave behaviors in two major SSW events in the summer mesosphere. In summary, MERRA-2 data in the mesosphere have repeatedly been applied in research on SSW events, and the data quality is very reliable.

The atmospheric parameters needed included temperature, geopotential, wind, and vertical pressure velocity. We used data provided through the following two websites: https://disc.gsfc.nasa.gov/datasets/M2I6NVANA_5.12.4/summary?keywords=merra-2 and https://disc.gsfc.nasa.gov/datasets/M2I3NVASM_5.12.4/summary?keywords=merra-2. The M2I6NVANA_5.12.4 data have a 6-hour resolution and include the parameters of temperature, wind speed, surface pressure, and specific humidity, whereas the M2I3NVASM_5.12.4 data have a 3-hour resolution and include the parameters of temperature, wind speed, vertical pressure velocity, and surface potential height. We use pressure and surface potential height data to calculate the geopotential. By combining the two datasets, we were able to obtain all the parameters needed. The data include 25 vertical levels, ranging from 10 to 0.01 hPa. We use a resolution of $0.5° \times 0.625°$ in the horizontal direction.

Figure 1 shows the variations in the polar temperature and zonal wind at 60°N at 10 hPa from November 24, 2022, to March 31, 2023, from the MERRA-2 database. Two obvious warming phases were observed. The zonal wind has reversed three times: on January 26–30, February 14–22, and February 24–March 9

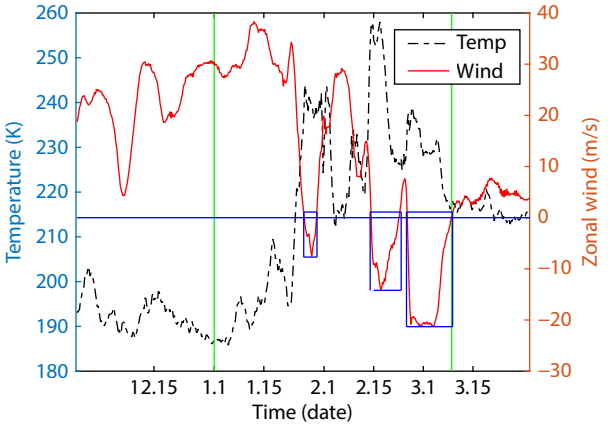

Figure 1. Variations in the polar temperature and zonal wind at 60°N at 10 hPa from November 24, 2022, to March 31, 2023, based on the MERRA-2 database. The SSW period is indicated by the vertical green lines. The three reversals of the zonal wind are marked with blue squares.

(marked with blue squares). According to the definition provided by the World Meteorological Organization, SSWs can be divided into major warmings and minor warmings. In addition to the temperature gradient reversal, major SSWs have a reversal of the zonal-mean wind from eastward to westward at 60° (Chandran and Collins, 2014). Therefore, this SSW is a major event. According to the period of temperature increase, we define this SSW period from January 1, 2023, to March 9, 2023 (marked with vertical green lines).

We apply the MWT and MS-ECT methods to analyze this SSW event. The MWT method was proposed by Liang XS and Anderson (2007) in an attempt to separate nonstationary processes while preserving spatial localization. It is a functional analysis tool that decomposes a functional space into a direct sum of orthogonal subspaces, each with an exclusive range of scales, while preserving its local properties. The subspace is called a scale window. The MWT method was developed to provide a faithful representation of the multiscale energies on the resulting scale windows and hence makes the MS-ECT analysis possible. In this framework, a functional space can be decomposed into several scales. Taking three scales as an example, a functional space $u(t)$ can then be written as

$$u(t) = \tilde{u}^{0}(t) + \tilde{u}^{1}(t) + \tilde{u}^{2}(t), \tag{1}$$

where $(\cdot)^{\tilde{}\varpi}$ denotes a subspace with ϖ being its index. In this work, $(\cdot)^{\tilde{}0}$ denotes the large-scale window, $(\cdot)^{\tilde{}1}$ denotes the SSW-scale window, and $(\cdot)^{\tilde{}2}$ denotes the synoptic-scale window. More detailed derivations are shown in Liang XS (2016).

The first step of the MWT is to determine the scales of subspaces. Because the MWT requires that the number of time steps be a power of 2, we choose the period from November 24, 2022, to March 31, 2023 (128 days, 2^7). The SSW event is included in this period. Because the resolution of data is 6 hours, the number of data points in this period is 512 (2^9).

The determination of scales can be achieved through the charac-

teristics of the SSW and the wavelet spectral analysis. During SSWs, the temperature increases sharply in a week or less. The entire SSW can last for 1 or 2 months (Butler et al., 2015). The variation in temperature at 10 hPa in this period and the wavelet spectrum of the period are shown in Figure 2. During the period of temperature increase, there are clearly two peaks. One is at 64 days and the other corresponds to a period of 16 days. Frequencies with a periodicity of 8 days also occur.

When separating scales, we aim to assign large-scale processes to represent background variations, mesoscale dynamics to capture the two distinct warming phases and wind reversals, and small-scale components to filter out weather noise. The determination of scale windows is based on the characteristic temporal scales of SSW events and is supported by the wavelet spectral analysis (Figure 2). The chosen thresholds are physically meaningful for the following reasons:

(1) **Large-scale window (>64 days):** This window captures the seasonal-scale background circulation, including the gradual evolution of the polar vortex and long-term trends. The multi-month scale is relevant for the preconditioning and slow recovery phases associated with SSWs (Butler et al., 2015).

(2) **SSW-scale window (8–64 days):** This window encompasses the full life cycle of an SSW event, from its initiation through its peak and subsequent decay, which typically spans several weeks to 2 months. It directly captures planetary wave activity with periods of ~10–30 days, which are the primary drivers of SSW dynamics (Baldwin et al., 2021). The wavelet spectrum (Figure 2) shows distinct peaks at periods of approximately 16 days and 8 days during the warming phases, firmly situating these dominant signals within this scale window.

(3) **Synoptic-scale window (<8 days):** This window filters higher frequency transients, including synoptic-scale weather disturbances and gravity waves. These processes can interact with the mean flow and planetary waves during SSWs, contributing to localized energy transfers and mesospheric effects (Tomikawa et al., 2012). The spectral power at periods below 8 days represents this background of higher frequency variability.

To assess potential edge effects arising from the fixed 128-day analysis window required for the MWT, we conduct a sensitivity test. The window is shifted forward and backward by ±3 days (i.e., analyzing periods from November 21, 2022, to March 28, 2023, and from November 27, 2022, to April 3, 2023). The MWT decomposition is repeated for these adjusted windows. The resulting scale-separated fields, particularly within the SSW-scale window during the core event period (January–March 2023), show highly consistent spatial patterns and magnitudes of energy terms compared with the original window. This result confirms that the chosen 128-day window does not introduce significant boundary artifacts that would affect the primary conclusions of this study.

On the basis of the MWT, we can form a localized multiscale energetics function from the original function, including temperature T, winds $\boldsymbol{v} = (u, v, w)$, and geopotential ϕ in the isobaric coordinate system. According to the definition of multiscale energy, the kinetic energy (KE) K^{ϖ} and the available potential energy (APE) A^{ϖ} in the ϖ subspace are

$$K^{\varpi} = \frac{1}{2}\left(\tilde{v}_h^{\varpi} \cdot \tilde{v}_h^{\varpi}\right), \tag{2}$$

$$A^{\varpi} = \frac{1}{2}c\left(\tilde{T}^{\varpi}\right)^2,\ c = \frac{g}{\overline{T}\left(\frac{g}{c_P} - L\right)}, \tag{3}$$

where v_h is the horizontal wind, g is the gravitational acceleration, c_P is the specific heat at constant pressure, and $L = -\partial\overline{T}/\partial z$ is the lapse rate. In addition, $\widetilde{(\cdot)}_h^{\varpi}$ denotes the MWT on the window at horizontal component h, and $\overline{(\cdot)}$ denotes the average value. The equations of energy balance can be inferred as

$$\frac{\partial K^{\varpi}}{\partial t} = -\nabla \cdot Q_K^{\varpi} - \nabla \cdot Q_P^{\varpi} - b^{\varpi} + \Gamma_K^{\varpi} + F_K^{\varpi}, \tag{4}$$

$$\frac{\partial A^{\varpi}}{\partial t} = -\nabla \cdot Q_A^{\varpi} + b^{\varpi} + S_A^{\varpi} + \Gamma_A^{\varpi} + F_A^{\varpi}. \tag{5}$$

where

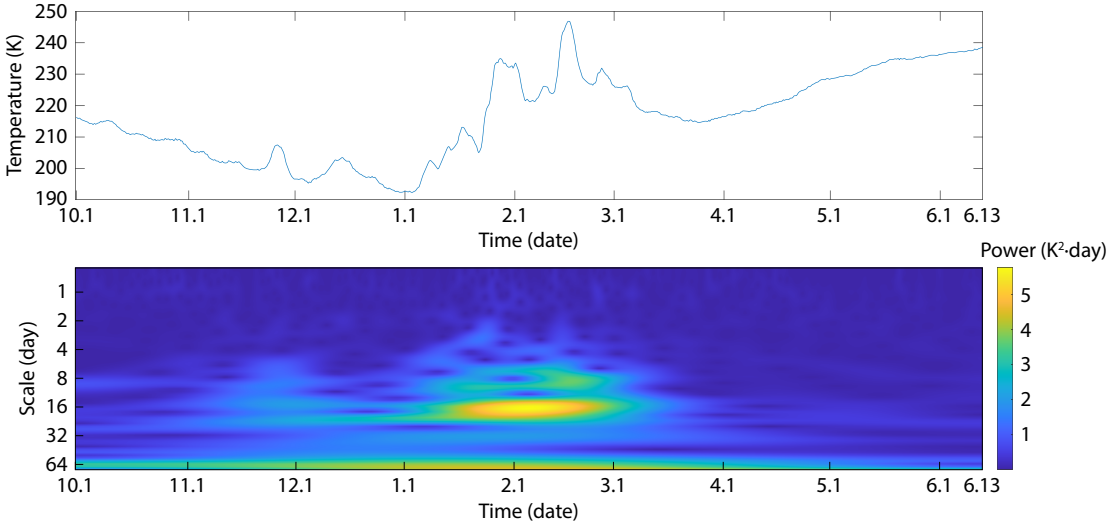

Figure 2. Top: Variation in the temperature at 10 hPa from October 1, 2022, to June 13, 2023. Bottom: Variation in the wavelet spectrum at 10 hPa from October 1, 2022, to June 13, 2023.

$$\frac{\partial K^{\varpi}}{\partial t} = \frac{1}{2}\frac{\partial}{\partial t}\left(\tilde{v}_h^{\varpi}\cdot\tilde{v}_h^{\varpi}\right)$$

and

$$\frac{\partial A^{\varpi}}{\partial t} = \frac{1}{2}\frac{\partial}{\partial t}\left(c\left(\tilde{\hat{T}}^{\varpi}\right)^2\right)$$

are the change rates of KE and APE respectively;

$$-\nabla\cdot Q_K^{\varpi} = -\frac{1}{2}\nabla\cdot\left[\widetilde{(vv_h)}^{\varpi}\cdot\tilde{v}_h^{\varpi}\right]$$

is the convergence of flux of KE on window ϖ;

$$-\nabla\cdot Q_P^{\varpi} = -\nabla\cdot\left[\tilde{\hat{v}}^{\varpi}\tilde{\hat{\Phi}}^{\varpi}\right]$$

is the convergence of pressure flux, where Φ is the geopotential function;

$$b^{\varpi} = \tilde{\hat{\omega}}^{\varpi}\tilde{\hat{\alpha}}^{\varpi}$$

is the buoyancy conversion, where $\omega = \frac{\mathrm{d}p}{\mathrm{d}t}, \alpha = \frac{R}{p}T$ is the specific volume;

$$\begin{aligned}\Gamma_K^{\varpi} =& \frac{1}{2}\left\{\widetilde{(vu)}^{\varpi}\cdot\nabla\tilde{u}^{\varpi} - \left[\nabla\cdot\widetilde{(vu)}^{\varpi}\right]\tilde{u}^{\varpi}\right\}\\ &+\frac{1}{2}\left\{\widetilde{(vv)}^{\varpi}\cdot\nabla\tilde{v}^{\varpi} - \left[\nabla\cdot\widetilde{(vv)}^{\varpi}\right]\tilde{v}^{\varpi}\right\}\end{aligned}$$

and

$$\Gamma_A^{\varpi} = \frac{1}{2}c\left[\widetilde{(v\hat{T})}^{\varpi}\cdot\nabla\tilde{\hat{T}}^{\varpi} - \tilde{\hat{T}}^{\varpi}\nabla\cdot\widetilde{(v\hat{T})}^{\varpi}\right]$$

are canonical transfers of KE and APE to window ϖ, respectively;

$$-\nabla\cdot Q_A^{\varpi} = -\frac{1}{2}\nabla\cdot\left[c\tilde{\hat{T}}^{\varpi}\widetilde{(v\hat{T})}^{\varpi}\right]$$

is the convergence of flux of APE on window ϖ;

$$S_A^{\varpi} = \frac{1}{2}\tilde{\hat{T}}^{\varpi}\widetilde{(\omega\hat{T})}^{\varpi}\frac{\partial c}{\partial p} + \frac{1}{\bar{T}}\widetilde{(\hat{\omega}\hat{\alpha})}^{\varpi}$$

is the apparent source–sink (usually negligible); and F_K^{ϖ} and F_A^{ϖ} are the frictional dissipation of KE and APE, respectively. For convenience, $\nabla\cdot Q_K^{\varpi}$, $\nabla\cdot Q_P^{\varpi}$, and $\nabla\cdot Q_A^{\varpi}$ are written as ΔQ_K^{ϖ}, ΔQ_P^{ϖ}, and ΔQ_A^{ϖ}, respectively. Above are expressions for energy per unit mass (with units of m^2/s^3). This is called the MS-ECT method.

Notably, the canonical transfers (Γ_K^{ϖ} and Γ_A^{ϖ}) are essential in the MS-ECT, which means the energy transfer between different subspaces. This energy transfer has an important property; that is, this kind of cross-scale transfer neither generates nor destroys energy, then it characterizes the redistribution of energy between different subspaces. The canonical APE transfer Γ_A^{ϖ} measures the rate of APE exchange between scales attributable to correlations between velocity and temperature gradients. In quasi-geostrophic theory, such a transfer is directly associated with baroclinic instability, which converts mean-state APE into eddy APE. Thus, a positive $\Gamma_A^{0\to1}$ indicates that baroclinic instability is transferring APE from the large-scale background to the SSW-scale disturbances. The canonical KE transfer and canonical APE transfer rigorously correspond to the barotropic instability process and baroclinic instability process in classical geophysical fluid dynamics while avoiding the global limitations inherent in classical theories. Consequently, these canonical energy transfers can authentically characterize both the temporal intermittency and spatial inherent spatial localization of fluid destabilization processes (Liang XS and Robinson, 2005).

3. Results

3.1 The Multiscale Results

The polar temperature and zonal wind at 60°N at 10 and 0.01 hPa and their three scale decompositions are shown in Figure 3. The temperature at 10 hPa has two periods of increase during the SSW period. The variation in temperature at 0.01 hPa is opposite that at 10 hPa. It decreases twice during the SSW period. As for the zonal wind, it reverses from eastward to westward around the middle of February at 10 hPa, indicating it is a major SSW. The zonal wind at 0.01 hPa also reverses at the same time, but from westward to eastward. The large scale roughly depicts the trends of temperature and zonal wind variations during this period. The SSW scale highlights two temperature increases and three zonal wind reversals at 10 hPa during the SSW period (from the end of January to the end of February in 2023). The synoptic scale shows the temperature variabilities attributable to synoptic disturbances.

At first, we study the variations in the original temperature and wind field during the SSW, as shown in Figure 3. According to the properties of temperature variations, we divide the duration of January 1, 2023, to March 31, 2023, into four subperiods: January 1–10 (precursor stage), January 10–February 5 (rapid warming stage), February 5–March 9 (maintenance stage), March 9–31 (decaying stage). We then focus on what occurs at SSW-scale temperatures and with zonal winds.

Figure 4 shows the SSW-scale temperatures and winds in the northern hemisphere in different subperiods. In the mesosphere, the warm air occupies the north pole during the precursor stage, and soon a cooling occurs during the maintenance stage. In the stratosphere, two warmings occur during the rapid warming stage and the maintenance stage. The zonal wind reverses to easterly in both the mesosphere and the stratosphere during the SSW period.

3.2 Results of the Multiscale Energetics Analysis

On the basis of the results for the MWT, the multiscale energetics are analyzed. The variations in temperature and zonal wind over time and height are first analyzed. Figures 5a and 5c show multiscale variations in the north pole temperature and a ~60°N–90°N mean zonal wind with height and time. It can be observed that as the time changes, the temperature decreases with increasing altitude. Three reversals in the raw zonal wind are observed from January 26 to 30, February 14 to 22, and February 24 to March 9, reaching a maximum altitude of 80 km in the mesosphere. Before analyzing the energy transfer, it is necessary to understand the overall energy variations. Figures 5b and 5d show multiscale variations in the 60°N–90°N mean APE and KE with altitude and time. Overall, the KE propagates downward over time from 60 to 40 km, indicating that the dynamic mechanism for reversal of the zonal wind is from the mesosphere. The changes in KE at the large and SSW scales are consistent with the changes in zonal wind at the large and SSW scales, as shown in Figure 5a. The SSW-scale KE exhibits a vertical "strip-like" distribution, and the SSW-scale zonal

wind shows a vertical strip-like distribution, indicating that the KE is highly correlated with the zonal wind. The SSW-scale APE is consistent with the SSW-scale temperature, with both showing a "point-like" distribution, indicating a high correlation between the APE and temperature. However, before January 15, a "fracture" occurs in the large-scale APE from 50 to 60 km, which divides the APE into two parts. This phenomenon does not occur in the large-scale temperature, zonal wind, and KE. This phenomenon is likely due to an energy exchange with regions outside the polar vortex, possibly through wave–mean flow interactions or lateral transport

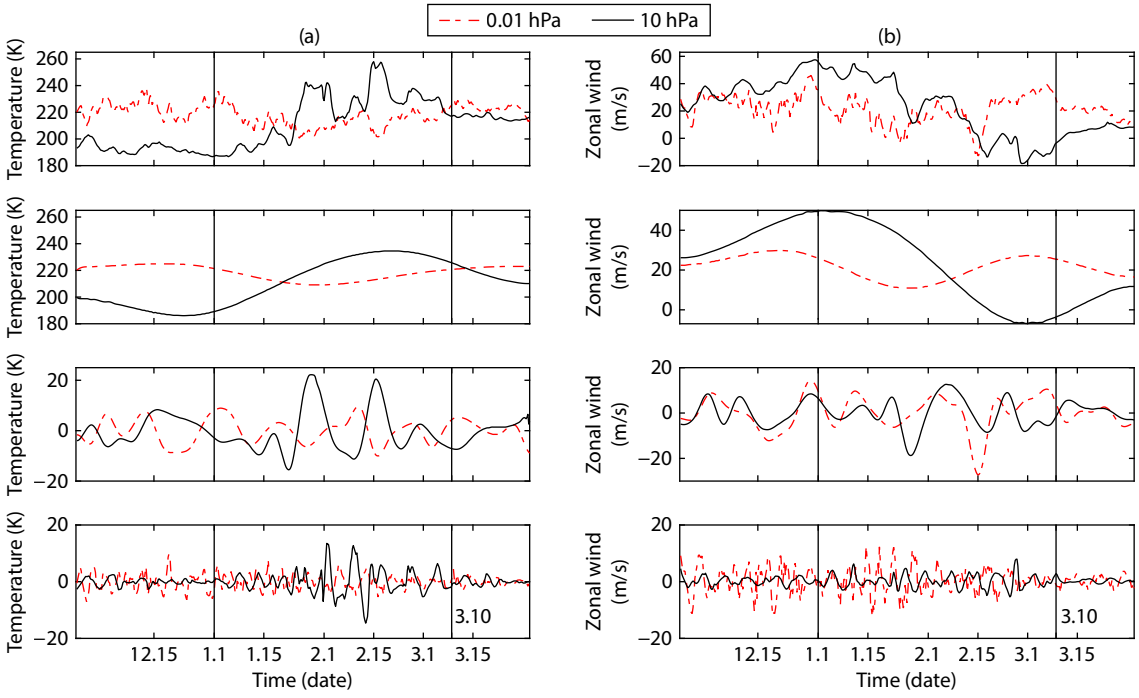

Figure 3. (a) From top to bottom: The raw polar temperature at 10 hPa (black) and 0.01 hPa (red) at the large scale, SSW scale, and synoptic scale. (b) The same as the left column but for zonal wind at 60°N. The SSW period occurs between the vertical black lines.

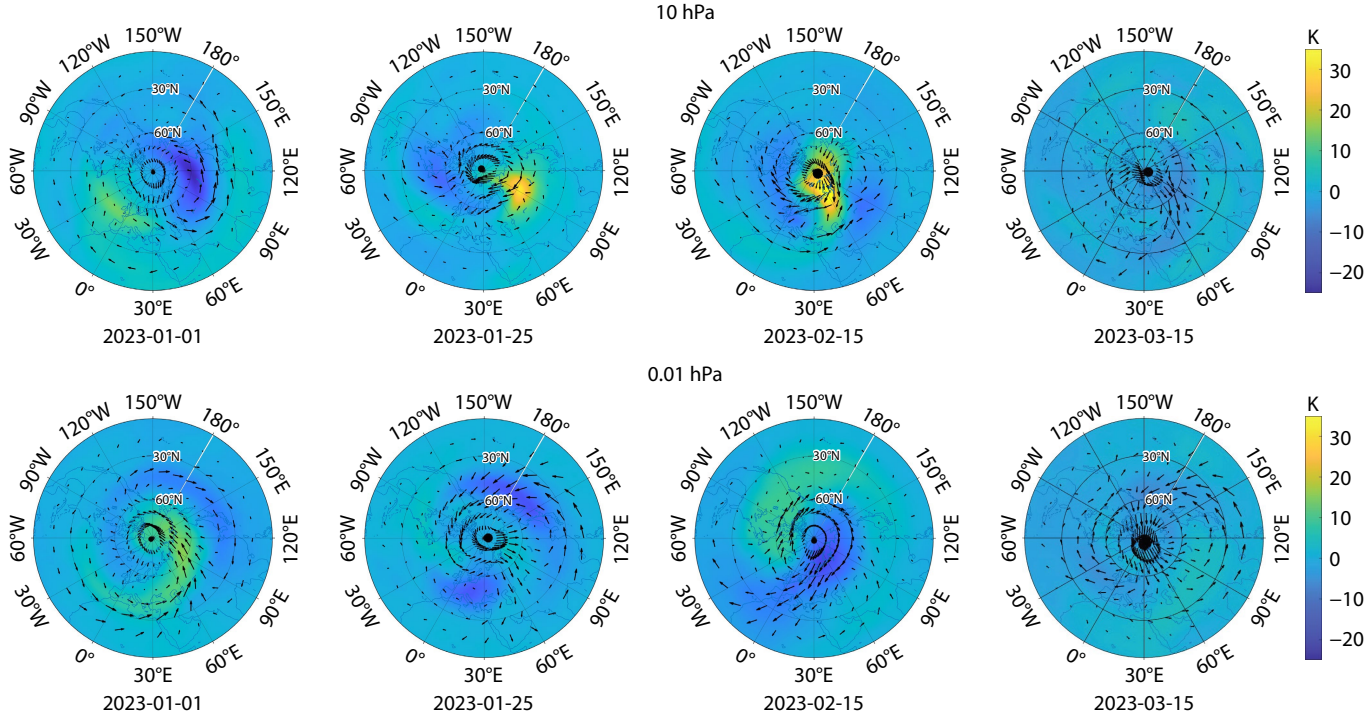

Figure 4. SSW-scale temperature (K) and wind (m/s) at 10 hPa (top row) and 0.01 hPa (bottom row) at different dates (e.g., 01-01 denotes January 1) in the northern hemisphere.

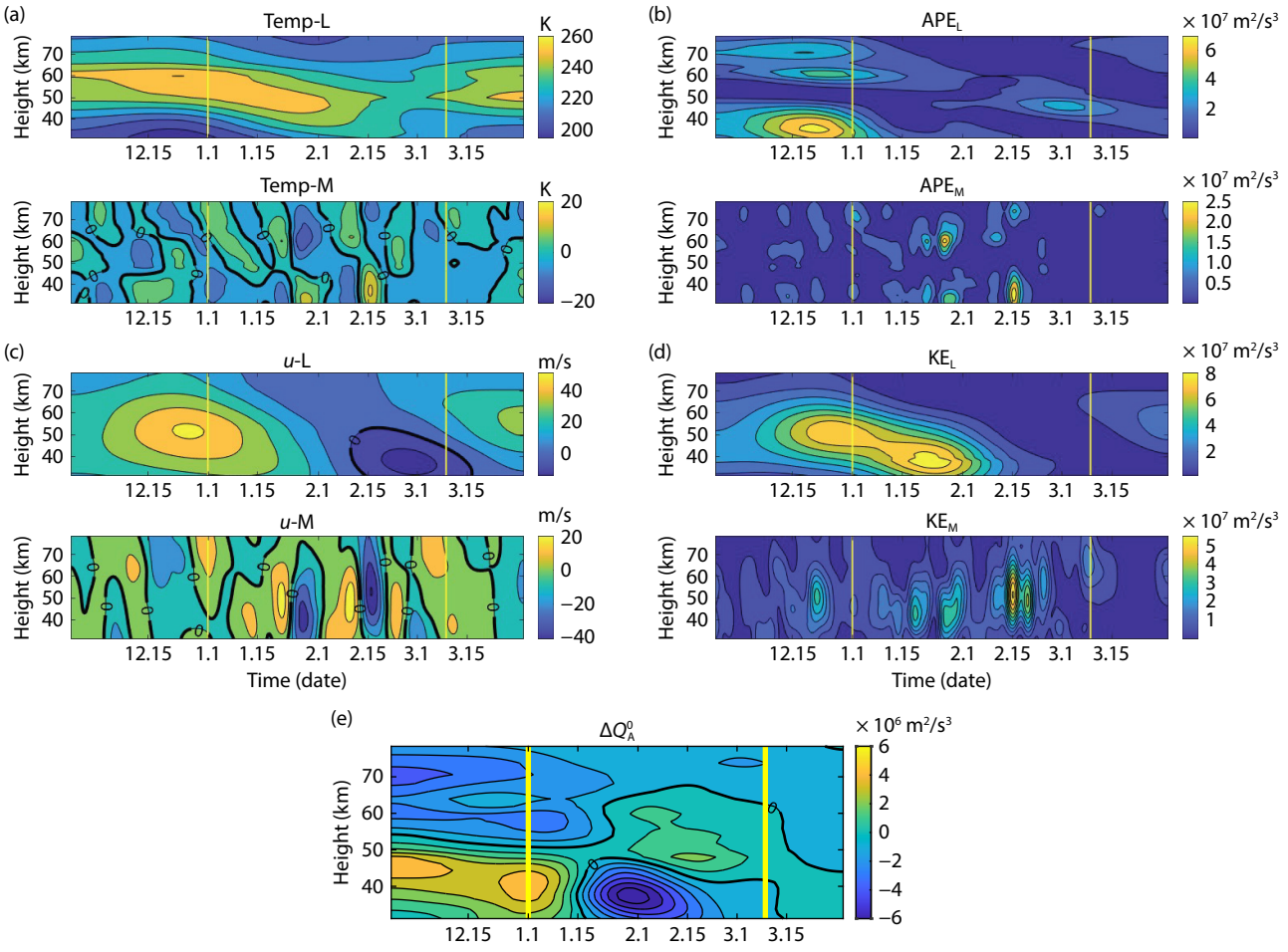

Figure 5. (a) Large-scale and SSW-scale variations in the north pole temperature with height and time (November 24–March 31). (b) The same as (a) for APE. (c) The same as (b) for the 60°N–90°N mean zonal wind. (d) The same as (b) for KE. (e) Large-scale variation in the ~60°N–90°N mean APE transport with height and time. The vertical yellow lines indicate the SSW period. The suffixes or subscripts L and M mean large-scale and SSW-scale variation, respectively.

from lower latitudes. Figure 5e shows the variation in ΔQ^0_A from latitude 60°N to the north pole with height and time, where ΔQ^0_A represents a convergence of the APE flux at the SSW scale. This variation shows that transport of the APE is divided into two parts before January 15 at a height of ~55 km, with negative values above 55 km, representing the transfer of energy from the outside to the APE, and positive values below 55 km representing the transfer of energy from the APE to the outside. The negative values of ΔQ^0_A correspond to erosion of the vortex shown in the stratosphere. In contrast, in the mesosphere, the positive values of ΔQ^0_A indicate a convergence of the APE vortex. Because SSWs are preceded by erosion of the vortex, which forms a "surf zone" surrounding the vortex (Baldwin et al., 2021), transport may be the reason for the fracture of the APE.

To investigate the energy coupling between the mesosphere and stratosphere, Figure 6 illustrates the vertical parts of APE transport, KE transport, and pressure flux. For large-scale dynamics, a demarcation at 60 km is evident prior to the occurrence of the SSW. Above 60 km, APE propagates upward, whereas below this altitude, APE exhibits downward propagation. Vertically, KE transport is predominantly mediated by pressure flux. During SSW events, below 60 km, the vertical component of pressure flux shifts upward, indicating that the vertical energy source for large-scale KE originates primarily from the lower atmosphere.

For SSW-scale dynamics, APE transport during both warming periods (January 25 and February 15) displays downward propagation, which may contribute to the energy supply driving the warming. Concurrently, KE transport during SSWs is predominantly downward, whereas pressure flux alternates between the downward and upward directions. This alternating pattern suggests active vertical energy exchange between the mesosphere and stratosphere, primarily facilitated by pressure flux.

To better compare the differences and similarities in energy transfer between the mesosphere and the stratosphere, we select two altitudes (0.01 hPa for the mesosphere and 10 hPa for the stratosphere) and analyze the variations in different energetic forms during the SSW event. Figures 7a and 7b show the variation in multiscale KE and APE over time at two altitudes. At 0.01 hPa, large-scale KE and APE increase before the SSW and decrease during the SSW. The SSW-scale KE and APE reach their maximum values around February 15, corresponding to a reversal of the

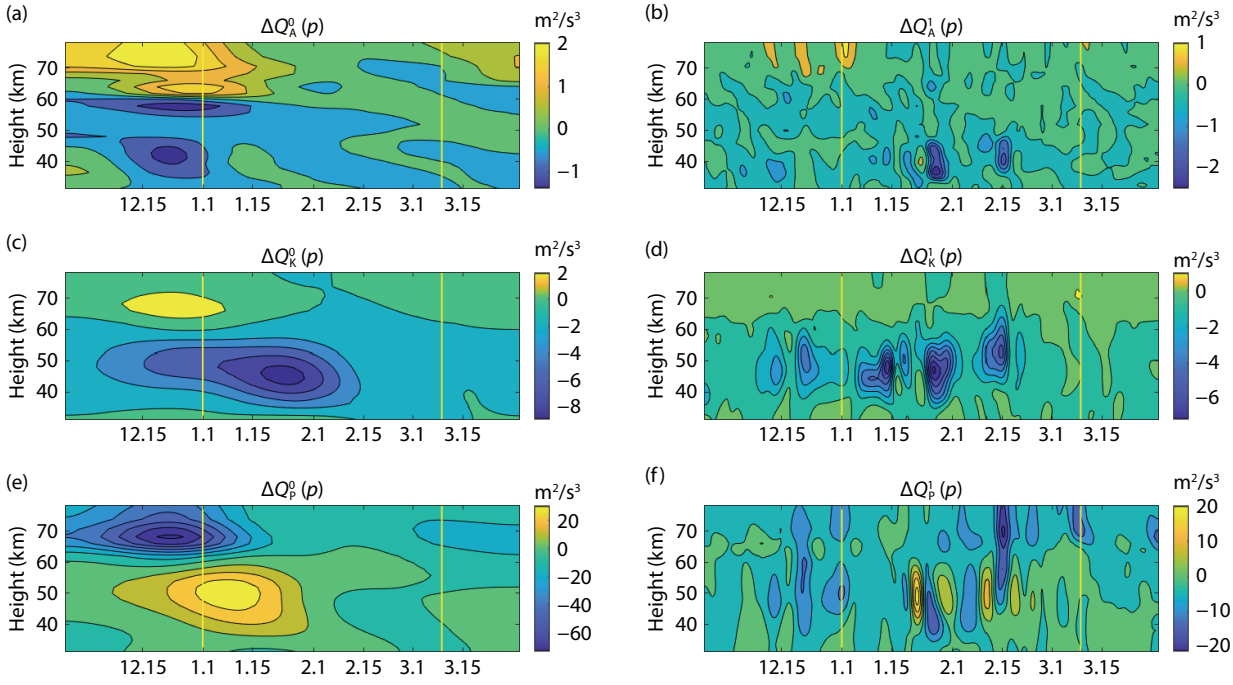

Figure 6. The vertical part of (a) large-scale APE transport, (b) SSW-scale APE transport, (c) large-scale KE transport, (d) SSW-scale KE transport, (e) large-scale pressure flux, and (f) SSW-scale pressure flux. The vertical yellow lines indicate the SSW period.

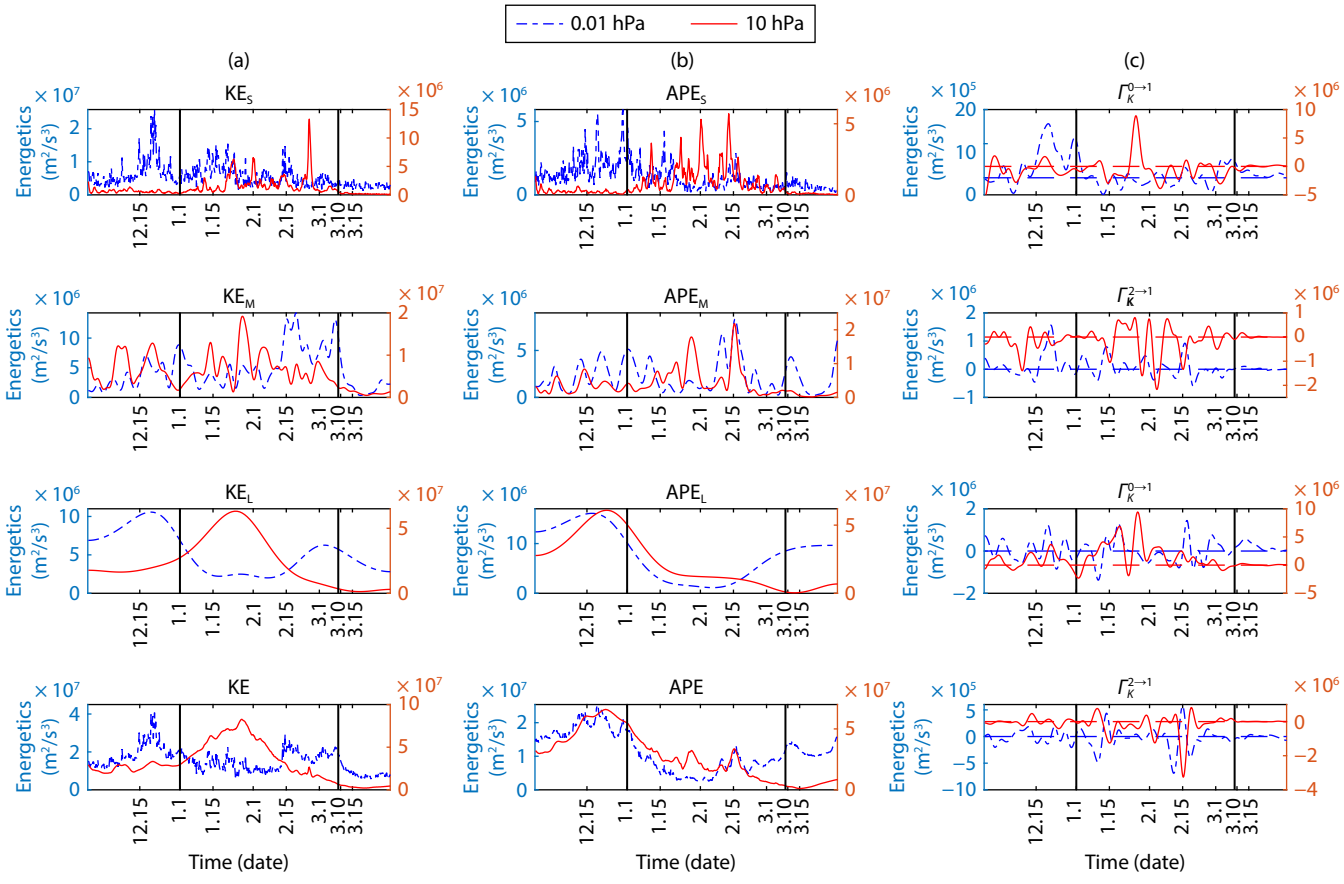

Figure 7. (a) Variation in multiscale KE over time at 0.01 hPa (dotted-dashed blue line) and 10 hPa (solid red line). From top to bottom: synoptic-scale (subscripts S), SSW-scale (subscripts M), large-scale (subscripts L), and raw data. (b) Same as (a), but for APE. (c) Variation in the canonical transfer over time; the dashed lines indicate zero. The SSW period occurs between the black lines.

zonal wind in the mesosphere and a decrease in temperature, respectively. Unlike the mesosphere, the large-scale KE increases during the SSW, whereas the SSW-scale KE reaches its maximum value around January 25, and the SSW-scale APE has two peaks around January 25 and February 15.

Figure 7c shows the variation in canonical transfer over time at two altitudes. At 0.01 hPa, before the occurrence of the SSW, the multiscale transfer direction of KE is mainly from large scale to SSW scale, and from synoptic scale to SSW scale, whereas the multiscale transfer direction of APE is relatively variable; during the SSW, the KE transmitted from synoptic scale to SSW scale has two peaks around January 15 and February 15, and the APE transmitted from large scale and synoptic scale to SSW scale also has two peaks around the dates mentioned. At 10 hPa, before the occurrence of the SSW, multiscale energy transfer is relatively stable, with the main amplitude occurring during the SSW. The transfer from large-scale to SSW-scale KE reaches its maximum on January 25, when the zonal wind has its first deceleration, followed by the transfer from SSW-scale to synoptic-scale KE, resulting in barotropic instability. On February 15, KE once again shows a transfer direction among large, SSW, and synoptic scales, corresponding to a reversal of the zonal wind, indicating a barotropic instability energy supply for the reversal of the zonal wind. On January 25, the APE term from large scale to SSW scale reaches its maximum, and the first warming energy is from large-scale APE. During the second warming (February 15), the APE from synoptic scale to SSW scale reaches its maximum, and the energy is from small-scale APE. The overall transmission direction is large scale → SSW scale → synoptic scale, indicating that the energy for two warmings is supplied by baroclinic instability.

Figures 8a–8c show the variations in APE transport, KE transport, and pressure flux with time at two altitudes. The energy transfer between APE and the outside is mainly achieved through the advection APE transport. At 0.01 hPa, the APE transport is similar to the KE transport. At 10 hPa, the large-scale APE transport is positive before the occurrence of the SSW (outward transport) and becomes negative after January 15, transmitting energy inward. The SSW-scale APE advection transport reaches its minima on January 25 and February 15, and the energy transmitted through advection is the highest. The advection APE transport provides an energy source for two periods of warming.

At 0.01 hPa, the large-scale pressure flux is positive overall and has a large amplitude, indicating that the transfer of KE to the outside is mainly from the work done by the pressure flux. The work done by the pressure flux to the outside is relatively small during the SSW. On January 2 and February 10, the SSW-scale pressure flux is negative, indicating that work is done to enhance the eddy KE at the expense of the mean flow, which facilitates the deceleration and eventual reversal of the zonal wind. At 10 hPa, the large-scale pressure flux is generally positive. But during the SSW, the pressure flux is relatively large. On January 25, the SSW-scale pressure flux applies work inward, providing energy for the KE and preparing energy for wind deceleration.

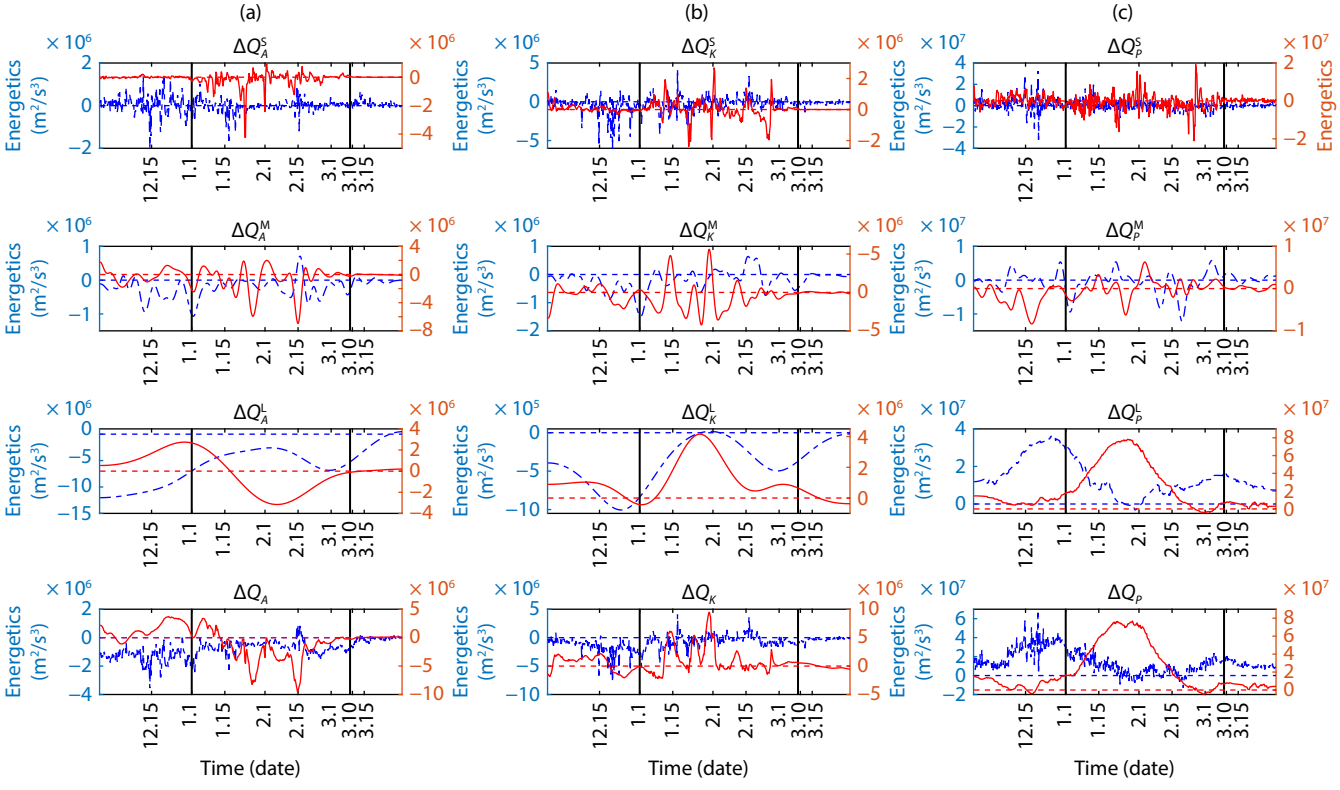

Figure 8. (a) Same as Figure 7a, but for APE transport at 0.01 hPa (dotted-dashed blue line) and 10 hPa (solid red line), and dashed lines indicate zero. (b) Same as Figure 7a, but for KE transport. (c) Same as Figure 7a, but for the convergence of pressure flux. The SSW period occurs between the black lines.

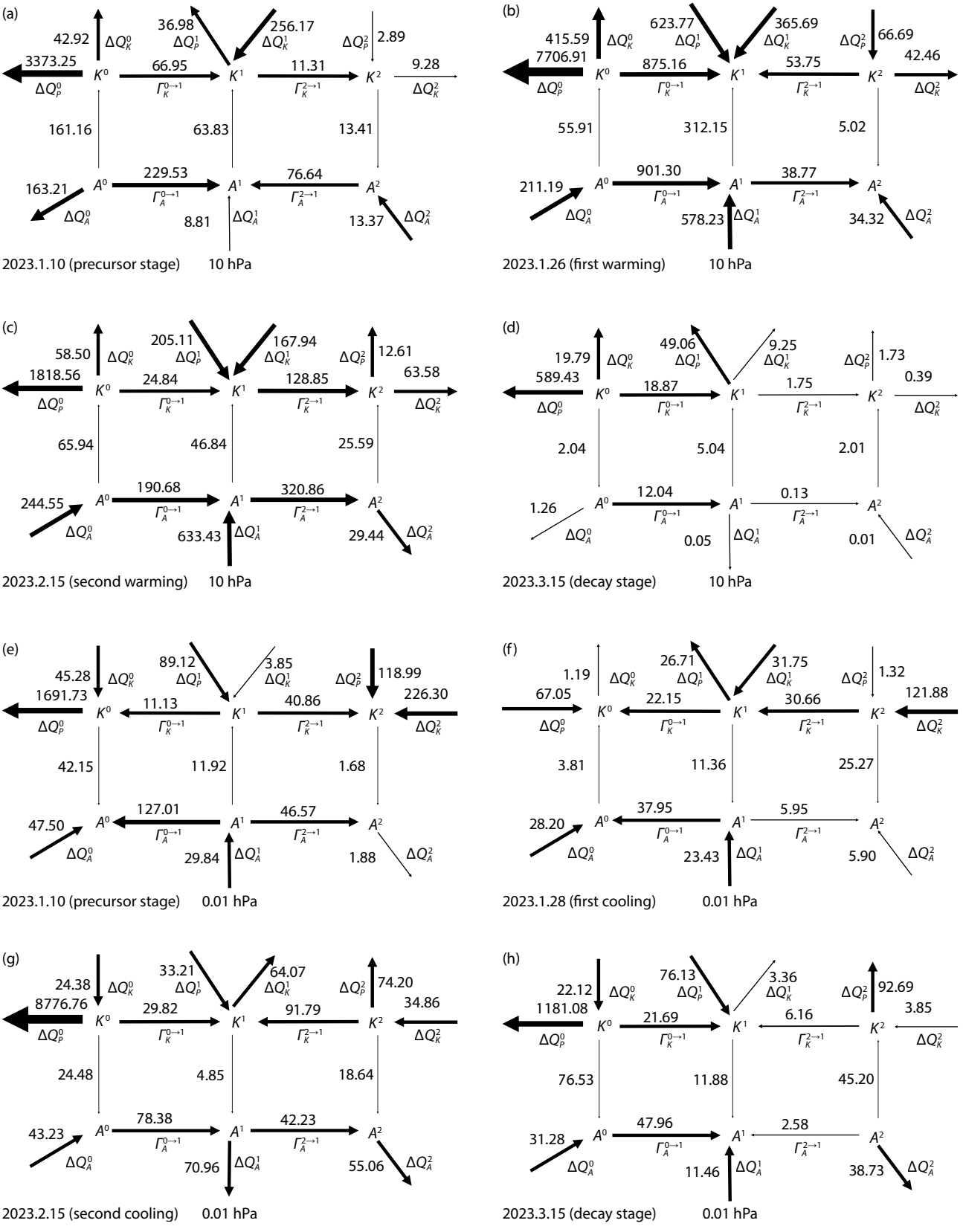

Figure 9. Charts of the typical multiscale energy cycles ($\times 10^4$ m^2/s^3, and buoyancy conversion is m^2/s^3) for the (a, e) precursor stage, (b, f) first cooling, (c, g) second cooling, and (d, h) decay stage at (a–d) 10 hPa and (e–h) ~0.01 hPa. The direction of the arrows indicates the direction of energy transfer and the thickness of the arrows indicates the relative magnitude of energy transfer.

The KE transport acts as both a source and sink of energy in the system. At 0.01 hPa, the negative large-scale KE transport indicates net energy inflow via advection. The decrease in its absolute value during the SSW suggests a reduction in the magnitude of this energy inflow, possibly owing to altered wave–mean flow interactions during the event. The SSW-scale KE transport is positive around February 20, during which KE flows out through advection transport. At 10 hPa, the large-scale KE transport is positive overall, meaning that KE flows out through advection transport. The amplitude of KE flowing out through advection transport increases during the SSW. The SSW-scale transport undergoes a change of first inflow and then outflow around January 15 and February 1. At this time, the exchange of KE with the outside world is more intense, and the zonal wind decreases sharply.

In different stages, the energy flow paths are quite different. We choose four significant dates to draw the energy flow charts at two respective heights. The results are shown in Figure 9. First, we focus on the stratosphere. At the precursor stage, both large-scale and synoptic-scale APE and APE transport ΔQ_A^1 provide energy for SSW-scale APE and prepare energy for the following rapid warming. The first warming coincides with the collaboration of the canonical APE transfer from A^0 through baroclinic instability and APE transport. The major energy sources for this warming are the transport ΔQ_A^1 and canonical transfer $\Gamma_A^{0\to1}$. The energy source of K^1 is through the transport ΔQ_K^1, the pressure work ΔQ_p^1, and canonical transfer from large-scale and synoptic-scale KE. At this point, K^1 stores a large amount of energy, reaching its peak, and the zonal wind correspondingly slows down to the first trough. During the second warming, the APE flow direction is similar to the first warming, indicating that the mechanism of this warming is the same as the first warming. As for the KE, the energy source is the collaboration of the canonical KE transfer from K^0 through barotropic instability, the transport ΔQ_K^1, and the pressure work ΔQ_p^1. At this time, the zonal wind reverses and reaches its maximum absolute value. The numerical value of energy flow decreases significantly at the decay stage.

The mesosphere has some differences in energy flow compared with those in the stratosphere. At the precursor stage, only ΔQ_A^1 provides energy for the SSW-scale APE. The first cooling is associated with the transport ΔQ_A^1, and the second cooling is associated with baroclinic instability. Little or no barotropic instability occurs for the KE during the entire SSW event. This is perhaps because the distribution of the zonal wind is relatively uniform in the mesosphere. During the zonal wind reversal period (Figure 9g), the energy source of K^1 is from both large-scale and synoptic-scale KE. The numerical value of energy flow significantly decreases at the decay stage as well.

4. Discussion

Through energetics analyses, we can compare the energy transfer mechanism and its effect on the temperature and zonal wind between different SSW events and altitudes. Figures 10a and 10b display the time evolution of the SSW-scale energetic terms accumulated over 60°N–90°N at 0.01–10 hPa for the 2023 SSW and the temperature variation at the north pole at two altitudes. As shown in Figures 10a and 10b, the APE balance on the SSW scale is mainly among baroclinic canonical transfer and transport. The canonical transfer contributes the most to the SSW-scale APE. For

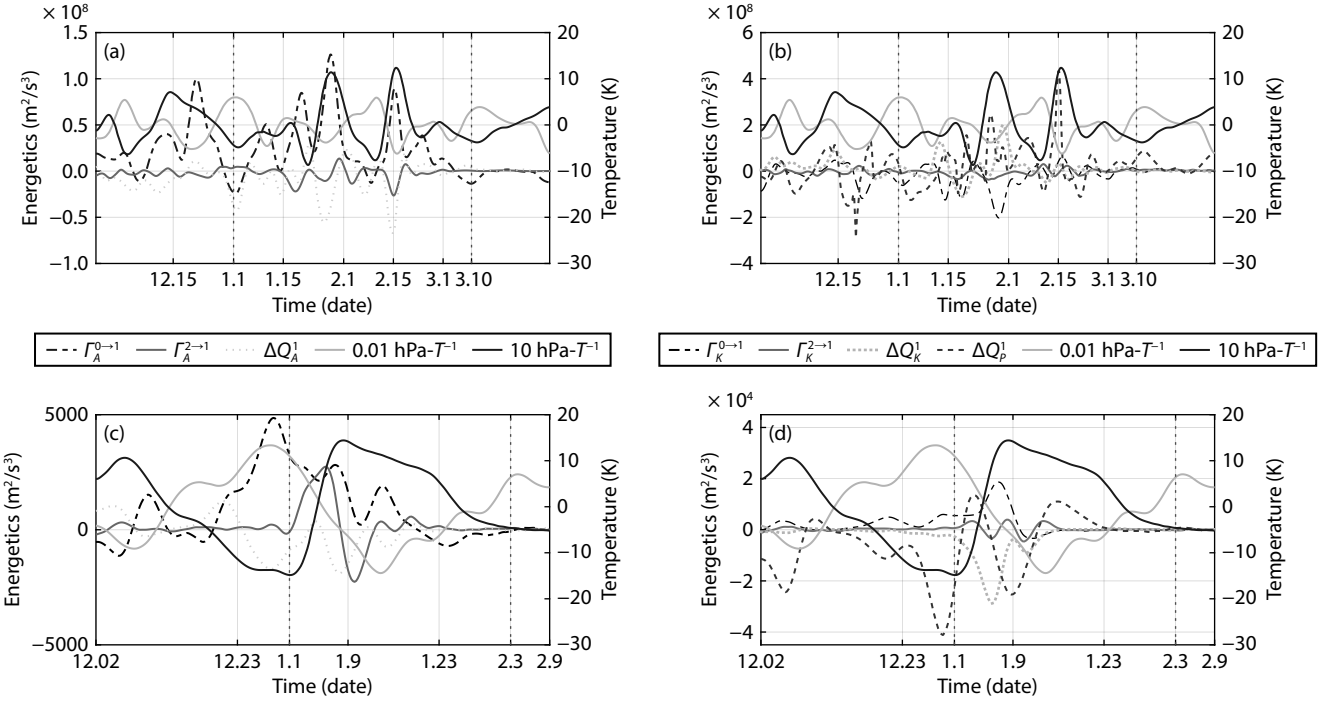

Figure 10. (a, b) Time evolution of the SSW-scale energetic terms accumulated over 60°N–90°N at 0.01–10 hPa for the 2023 SSW. (c, d) Same as (a) and (b) but for the 2012–2013 SSW. 0.01 hPa T^1 denotes the SSW-scale temperature at the 0.01 hPa pressure level; 10 hPa T^1 denotes the SSW-scale temperature at the 10 hPa pressure level.

the SSW-scale KE, the balance is mainly among the pressure fluxes ΔQ_P^1. We can also see that the SSW-scale temperature at 10 hPa generally follows the canonical transfer of APE ($\Gamma_A^{0\to1}$) and the variation in ΔQ_P^1 but that it is out of phase with the transport of SSW-scale APE (ΔQ_A^1) from January 25 to February 20.

Different SSW events exhibit distinct characteristics, and no universally accepted consensus has yet been established. Therefore, detailed investigations of typical cases remain essential. To identify systematic patterns in energy transport during SSWs, we conduct a comparative analysis of two distinct SSW events: 2023 SSW and 2012–2013 SSW. Both the 2023 and 2012–2013 SSWs are major SSWs. The 2012–2013 SSW lasted for an extraordinarily long time (2 months). It is unique in that, prior to the major warming, two minor warmings occurred in December 2012. The 2023 SSW also lasted for a long time (nearly 3 months) and two warmings also occurred. To compare the differences and similarities between the different SSW events, we analyze energetic variations in the 2012–2013 SSW in the middle atmosphere (the same SSW event explored by Xu F and Liang XS (2017); they also used the multiscale energy method to analyze this SSW event). Figures 10c and 10d display the time evolution of the SSW-scale energetic terms in the 2012–2013 SSW. An obvious result is that the energy terms are relatively smaller than those in the 2023 SSW. This difference is likely because the temperature had increased twice by a total of ~70° in the 2023 SSW (see Figure 1), whereas it had increased only once and by a total of ~40° in the 2012–2013 SSW. Moreover, the canonical transfer of APE ($\Gamma_A^{0\to1}$) is positive during warming; that is, the direction of the canonical transfer of APE is always through baroclinic instability in both SSWs.

To quantitatively assess the relative contributions of different processes to the SSW-scale APE variations, we calculate correlation coefficients between the APE changes and their major source terms $\Gamma_A^{0\to1}$, $\Gamma_A^{2\to1}$, and ΔQ_A^1. For the 2023 SSW, the correlation between APE changes and $\Gamma_A^{0\to1}$ is strikingly high (r = 0.90), whereas its correlation with the advective flux convergence (ΔQ_A^1) is r = −0.61. This finding indicates that the canonical transfer from the large-scale window explains approximately 81% (i.e., 0.9^2) of the variance in the SSW-scale APE growth, quantitatively confirming its dominant role. The negative correlation with advection suggests that the advective export of APE often occurs during phases of APE increase driven by baroclinic instability. A similar pattern holds for the 2012–2013 SSW, with $\Gamma_A^{0\to1}$ showing a high correlation (r = 0.87) and advection a strong negative correlation (r = −0.87). An interesting finding is that the canonical transfer from the synoptic-scale window ($\Gamma_A^{2\to1}$) shows a moderate negative correlation in 2023 (r = −0.62) and a weak one in 2012–2013 (r = −0.20), indicating it is not a primary source for the SSW-scale APE accumulation. These statistical metrics robustly support our conclusion that baroclinic instability, acting through the canonical transfer $\Gamma_A^{0\to1}$, is the principal driver of APE variability during these major SSWs, whereas advective processes largely act as a counterbalancing sink or spatial redistributor.

Because planetary-scale waves can be generated spontaneously by baroclinic instability (Hartmann, 1979; Domeisen and Plumb, 2012), this result confirms the propagation of planetary waves in SSWs at 10 and 0.01 hPa. The SSW-scale temperature at 10 hPa generally follows the canonical transfer of APE ($\Gamma_A^{0\to1}$), which is similar to that of the 2023 SSW event. It can be inferred that the variation in temperature is associated with the canonical transfer. However, the variation in ΔQ_P^1 seems different from that of the 2023 SSW event because no correlation with temperature is displayed. This difference may arise from event-specific external forcing or variations in nonlocal energy transport that modulate the pressure flux convergence.

As for the energy flow, some differences also exist between the different SSW events. In the 2012–2013 SSW, the pressure work ΔQ_P^0 always provides energy for K^0; however, the direction of the pressure work ΔQ_P^0 totally reverses in the 2023 SSW event. The large-scale KE mainly dissipates through pressure work. This dissipation is probably due to the different pressure distributions during the different SSW events.

In the stratosphere, we found that buoyancy conversion is important and that the SSW-scale temperature generally follows the variation in the pressure working rate but is out of phase with the APE transport (ΔQ_A^1) on the SSW window from 100 to 10 hPa (see Figure 10 in Xu F and Liang XS, 2017). As for the similarities, the direction of canonical transfer of APE is always from large scale to SSW scale through baroclinic instability in the stratosphere and mesosphere. From January 25 to February 20, the APE transport (ΔQ_A^1) is out of phase with the SSW-scale temperature in both the stratosphere and the mesosphere; that is, the outer transfer of APE is correlated with the SSW-scale temperature in the stratosphere and mesosphere.

Although our analysis highlights the importance of APE transport and baroclinic instability in the mesospheric cooling observed during the 2023 SSW, we note that other physical processes may also have contributed. For example, gravity wave drag can drive residual circulation that leads to adiabatic cooling, and nonlocal radiative cooling resulting from CO_2 emission is a persistent energy loss mechanism in the mesosphere. These processes are not explicitly separated in our energetic budget but are partly absorbed in the residual terms (e.g., F_K^{ϖ}, F_A^{ϖ}) and in the reanalysis thermodynamics. Future studies using high-resolution models that explicitly resolve gravity waves and interactive radiation would help quantify the relative roles of these mechanisms in concert with the energy transfer pathways identified here.

Regarding the reliability of MERRA-2 data in the mesosphere, it is noteworthy that several recent studies have utilized MERRA-2 reanalysis data to investigate dynamic processes in the MLT region during SSW events. For instance, Gong Y et al. (2025) utilized MERRA-2 data to analyze diurnal tidal variations in the MLT region during the 2020 SSW, demonstrating its applicability in capturing mesospheric wind and temperature structures. Similarly, Yang JF et al. (2017) used MERRA wind data to investigate the longitudinal and event-specific responses of zonal winds from the stratosphere to the lower thermosphere during several SSW events. Koushik et al. (2020) used MERRA-2 data to examine tropical stratopause zonal winds during major SSWs, validating the reanal-

ysis against Rocketsonde observations up to ~65 km. Becker and Oberheide (2023) also utilized MERRA-2 data to identify nonmigrating tidal components in the southern summer mesosphere, further supporting its utility in mesospheric studies. Although the MERRA-2 reanalysis has been widely used for mesospheric studies, its vertical resolution (25 levels from 10 to 0.01 hPa) is relatively coarse for resolving fine vertical gradients. Moreover, above ~70 km, reanalysis uncertainties grow because of sparse direct observations and greater model influence. Therefore, although the qualitative features of energy fluxes (e.g., direction of transfer, phase relationships) are considered robust, their quantitative magnitudes in the upper mesosphere (especially near 0.01 hPa) should be viewed with appropriate caution.

It is important to acknowledge the limitations of MERRA-2 in the mesosphere. Above ~60 km, direct observations become sparse, and reanalysis fields rely more heavily on model physics and prior forecasts. This necessity can introduce uncertainties in derived variables such as vertical motion and temperature gradients, which propagate into the computed energy fluxes. Although the overall patterns of energy transfer (e.g., sign of fluxes, scale-to-scale directions) are likely credible, their exact magnitudes near 0.01 hPa should be interpreted with caution. Future work using high-resolution models or enhanced observational datasets would help to better quantify mesospheric energetics during SSWs. Therefore, although the qualitative features and trends in the mesosphere are considered robust, quantitative interpretations in the 60–80 km region should be made with caution.

5. Conclusions

The 2023 SSW from January 1 to March 9 has two obvious temperature warming peaks and three zonal wind reversals. To clarify the energy transfer processes during SSWs to better understand the dynamic coupling of the middle atmosphere, we adopt the MWT and the MWT-based MS-ECT to investigate this major 2023 SSW event. We reconstruct the fields on three orthogonal subspaces, that is, a large-scale window (>64 days), an SSW window (8–64 days), and a synoptic-scale window (<8 days). The energetic transfer in the mesosphere is analyzed and compared with that in the stratosphere in the 2012–2013 SSW. The main conclusions can be summarized as follows:

(1) On the vertical transfer aspect, the KE transfers downward before the SSW. Pressure flux plays a critical role in coupling the mesosphere and stratosphere during SSW events.

(2) On the energetic flow paths, the SSW-scale KE has three different energy sources for the following warming, and both barotropic instability and baroclinic instability provide KE and APE in the stratosphere. In the mesosphere, a main energy source, APE transport ΔQ_A, provides the cooling, and baroclinic instability provides the APE.

(3) The energy terms of the 2012–2013 SSW event in the mesosphere are relatively smaller than those in 2023 SSW event. Although the specific energy flow paths vary between SSW events, a consistent feature is the dominant role of baroclinic instability in transferring APE from large-scale to SSW-scale windows in both the stratosphere and mesosphere. This feature suggests a robust mechanism underlying SSW dynamics, despite event-specific differences in external forcing or the background state. In both SSWs, energetic term fluctuations increase when the temperature changes. Moreover, baroclinic instability always exists during warming in both SSWs.

Through these energy transfer results derived from the SSW events, we have obtained a better understanding of the conversions between different energy sources and have learned about physical mechanisms of multilevel interactions and transformations in the middle atmosphere. However, this study also has certain limitations. First, the energetic diagnostics are derived entirely from reanalysis data (MERRA-2). Although MERRA-2 is reliable for large-scale stratospheric dynamics, its uncertainty increases in the mesosphere, and the vertical resolution is coarse for resolving fine-scale gravity wave processes. Second, the MWT framework assumes orthogonality between scale windows, which is a mathematical convenience that may not fully hold for nonlinear, interacting geophysical flows. Nevertheless, the MWT provides a robust and localizable decomposition suitable for diagnosing scale interactions in transient events like SSWs. Future work utilizing higher resolution models and constrained by dedicated mesospheric observations will help validate and refine the energy pathways identified here. Several issues still remain. First, the mechanisms between energetic transfers and atmospheric variations are deserving of study. Moreover, one may wonder about the underlying relationship between the energy in the stratosphere and that in the mesosphere. A possible approach is studying the energetic flow in more previous SSW events that include a greater range of height. We will explore these problems in future studies.

Data Availability

We acknowledge NASA's GMAO for providing the MERRA-2 reanalysis data via the websites https://disc.gsfc.nasa.gov/datasets/M2I6NVANA_5.12.4/summary?keywords=merra-2 and https://disc.gsfc.nasa.gov/datasets/M2I3NVASM_5.12.4/summary?keywords=merra-2.

Acknowledgments

This work was funded by the National Natural Science Foundation of China (NSFC Grant Nos. 12241101, 42174192, and 12573066).

References

Baldwin, M. P., Ayarzagüena, B., Birner, T., Butchart, N., Butler, A. H., Charlton-Perez, A. J., Domeisen, D. I. V., Garfinkel, C. I., Garny, H., … Pedatella, N. M. (2021). Sudden stratospheric warmings. *Rev. Geophys.*, *59*(1), e2020RG000708. https://doi.org/10.1029/2020RG000708

Becker, E., and Oberheide, J. (2023). Unexpected DE3 tide in the southern summer mesosphere. *Geophys. Res. Lett.*, *50*(20), e2023GL104368. https://doi.org/10.1029/2023GL104368

Butler, A. H., Seidel, D. J., Hardiman, S. C., Butchart, N., Birner, T., and Match, A. (2015). Defining sudden stratospheric warmings. *Bull. Amer. Meteor. Soc.*, *96*(11), 1913–1928. https://doi.org/10.1175/BAMS-D-13-00173.1

Chandran, A., and Collins, R. L. (2014). Stratospheric sudden warming effects on

winds and temperature in the middle atmosphere at middle and low latitudes: A study using WACCM. *Ann. Geophys.*, *32*(7), 859–874. https://doi.org/10.5194/angeo-32-859-2014

Chen, X., Hu, X., and Xiao, C. (2012). Variability of MLT winds and waves over mid-latitude during the 2000/2001 and 2009/2010 winter stratospheric sudden warming. *Ann. Geophys.*, *30*(6), 991–1001. https://doi.org/10.5194/angeo-30-991-2012

Domeisen, D. I. V., and Plumb, R. A. (2012). Traveling planetary-scale Rossby waves in the winter stratosphere: The role of tropospheric baroclinic instability. *Geophys. Res. Lett.*, *39*(20), L20817. https://doi.org/10.1029/2012GL053684

Eswaraiah, S., Jeong-Han Kim, Wonseok Lee, Junyoung Hwang, Kondapalli Niranjan Kumar, and Yong Ha Kim. (2020). Unusual Changes in the Antarctic Middle Atmosphere During the 2019 Warming in the Southern Hemisphere. *Geophysical Research Letters.*, *47*(19), e2020GL089199. https://doi.org/10.1029/2020GL089199

Gelaro, R., McCarty, W., Suárez, M. J., Todling, R., Molod, A., Takacs, L., Randles, C. A., Darmenov, A., Bosilovich, M. G., … Zhao, B. (2017). The modern-era retrospective analysis for research and applications, version 2 (MERRA-2). *J. Climate*, *30*(14), 5419–5454. https://doi.org/10.1175/JCLI-D-16-0758.1

Gong, Y., Bao, J. X., Zhang, S. D., Ma, Z., Zhou, Q. H., and Luo, J. H. (2025). A study of the diurnal tide in the MLT region during the 2020 sudden stratospheric warming over Yinchuan, China (38.8°N, 106.8°E). *J. Geophys. Res.: Space Phys.*, *130*(1), e2024JA033427. https://doi.org/10.1029/2024JA033427

Hartmann, D. L. (1979). Baroclinic instability of realistic zonal-mean states to planetary waves. *J. Atmos. Sci.*, *36*(12), 2336–2349. https://doi.org/10.1175/1520-0469(1979)036<2336:BIORZM>2.0.CO;2

Julian, P. R., and Labitzke, K. B. (1965). A study of atmospheric energetics during the January–February 1963 stratospheric warming. *J. Atmos. Sci.*, *22*(6), 597–610. https://doi.org/10.1175/1520-0469(1965)022<0597:ASOAED>2.0.CO;2

Kalisch, S., and Chun, H. Y. (2021). AIRS satellite observations of gravity waves during the 2009 sudden stratospheric warming event. *J. Geophys. Res.: Atmos.*, *126*(4), e2020JD034073. https://doi.org/10.1029/2020JD034073

Kohma, M., Sato, K., Nishimura, K., and Tsutsumi, M. (2021). Weakening of polar mesosphere winter echo and turbulent energy dissipation rates after a stratospheric sudden warming in the Southern Hemisphere in 2019. *Geophys. Res. Lett.*, *48*(10), e2021GL092705. https://doi.org/10.1029/2021GL092705

Koushik, N., Kumar, K. K., and Siddiqui, T. A. (2020). Westward acceleration of tropical stratopause zonal winds during major sudden stratospheric warming events. *Geophys. Res. Lett.*, *47*(3), e2019GL086857. https://doi.org/10.1029/2019GL086857

Li, Q. R., Zhang, S. D., Huang, K. M., Huang, C. M., Gong, Y., Tang, W. T., and Ma, Z. (2024). Long-term variation of arctic sudden stratospheric warmings (SSW) and potential causes. *Earth Planet. Phys.*, *8*(5), 742–752. https://doi.org/10.26464/epp2024037

Tang, L., Gu, S. Y., Teng, C. K. M., Yang, Z. L., Zhao, S. Y., Huang, H., and Wang, D. (2023). On the different quasi-2-day wave behaviors during sudden stratospheric warming periods. *Atmosphere.*, *14*(3), 521. https://doi.org/10.3390/atmos14030521

Liang, X. S., and Robinson, A. R. (2005). Localized multiscale energy and vorticity analysis. *Dyn. Atmos. Oceans*, *38*(3–4), 195–230. https://doi.org/10.1016/j.dynatmoce.2004.12.004

Liang, X. S., and Anderson, D. G. M. (2007). Multiscale window transform. *Multiscale Model. Simul.*, *6*(2), 437–467. https://doi.org/10.1137/06066895X

Liang, X. S. (2016). Canonical transfer and multiscale energetics for primitive and quasigeostrophic atmospheres. *J. Atmos. Sci.*, *73*(11), 4439–4468. https://doi.org/10.1175/JAS-D-16-0131.1

Lorenz, E. N. (1955). Available potential energy and the maintenance of the general circulation. *Tellus A*, *7*(2), 157–167. https://doi.org/10.3402/tellusa.v7i2.8796

Ma, J. W., and Liang, X. S. (2023). Upstream–downstream asymmetry in multiscale interaction underlying the Northern Hemisphere atmospheric blockings. *J. Atmos. Sci.*, *80*(8), 1995–2011. https://doi.org/10.1175/JAS-D-22-0220.1

Ma, Z., Gong, Y., and Zhang, S. D. (2024). Recent research progress on planetary waves in the middle and upper atmosphere during sudden stratospheric warmings. *Rev. Geophys. Planet. Phys. (in Chinese)*, *55*(1), 109–119. https://doi.org/10.19975/j.dqyxx.2022-076

Mitra, G., Guharay, A., Batista, P. P., and Buriti, R. A. (2022). Impact of the September 2019 minor sudden stratospheric warming on the low-latitude middle atmospheric planetary wave dynamics. *J. Geophys. Res.: Atmos.*, *127*(1), e2021JD035538. https://doi.org/10.1029/2021JD035538

Noguchi, S., Mukougawa, H., Kuroda, Y., Mizuta, R., Yabu, S., and Yoshimura, H. (2016). Predictability of the stratospheric polar vortex breakdown: An ensemble reforecast experiment for the splitting event in January 2009. *J. Geophys. Res.: Atmos.*, *121*(7), 3388–3404. https://doi.org/10.1002/2015JD024581

Plumb, R. A., (1981). Instability of the distorted polar night vortex: A theory of stratospheric warmings. *J. Atmos. Sci.*, 38, 2514–2531. https://doi.org/10.1175/1520-0469(1981)038<2514:IOTDPN>2.0.CO;2.

Roy, R., and Kuttippurath, J. (2022). The dynamical evolution of sudden stratospheric warmings of the Arctic winters in the past decade 2011–2021. *SN Appl. Sci.*, *4*(4), 105. https://doi.org/10.1007/s42452-022-04983-4

Scherhag, R. (1952). Die Explosionsartige Stratosphärenerwärmung Des Spätwinters 1951/52. *Berichte des Deutschen Wetterdienstes in der US-Zone, 6*(38), 51–63.

Tomikawa, Y., Sato, K., Watanabe, S., Kawatani, Y., Miyazaki, K., and Takahashi, M. (2012). Growth of planetary waves and the formation of an elevated stratopause after a major stratospheric sudden warming in a T213L256 GCM. *J. Geophys. Res.: Atmos.*, *117*(D16), D16101. https://doi.org/10.1029/2011JD017243

Trenberth, K. E. (1973). Dynamic coupling of the stratosphere with the troposphere and sudden stratospheric warmings. *Mon. Wea. Rev.*, *101*(4), 306–322. https://doi.org/10.1175/1520-0493(1973)101<0306:DCOTSW>2.3.CO;2

Wang, M. L., and Liang, X. S. (2022). Dynamical processes underlying a warm-sector rainstorm in Southern Fujian. *J. Trop. Meteor. (in Chinese)*, *38*(3), 467–480. https://doi.org/10.16032/j.issn.1004-4965.2022.042

Wargan, K., Labow, G., Frith, S., Pawson, S., Livesey, N., and Partyka, G. (2017). Evaluation of the ozone fields in NASA's MERRA-2 reanalysis. *Journal of Climate*., 30(8), 2961–2988. https://doi.org/10.1175/JCLI-D-16-0699.1

Wei, J. N., and Zhang, J. (2021). Influence of the position and kinetic energy anomalies of the inlet region of the Asian-African subtropical westerly jet on the mid-summer interdecadal drought in North China. *Plateau Meteor. (in Chinese)*, *40*(2), 281–291. https://doi.org/10.7522/j.issn.1000-0534.2020.00043

Wüst, S., and Bittner, M. (2011). Resonant interaction between two planetary waves as a precursor for stratospheric warmings?. *J. Atmos. Sol.-Terr. Phys.*, *73*(7–8), 771–778. https://doi.org/10.1016/j.jastp.2011.01.004

Xu, F., and Liang, X. S. (2017). On the generation and maintenance of the 2012/13 sudden stratospheric warming. *J. Atmos. Sci.*, *74*(10), 3209–3228. https://doi.org/10.1175/JAS-D-17-0002.1

Yang, J. F., Xiao, C. Y., Hu, X., and Xu, Q. C. (2017). Responses of zonal wind at ~40°N to stratospheric sudden warming events in the stratosphere, mesosphere and lower thermosphere. *Sci. China Technol. Sci.*, *60*(6), 935–945. https://doi.org/10.1007/s11431-016-0310-8

Yang, J. F., Wang, J. M., Liu, D., Guo, W. J., and Zhang, Y. M. (2024). Observation and simulation of neutral air density in the middle atmosphere during the

2021 sudden stratospheric warming event. *Atmos. Chem. Phys.*, *24*(17), 10113–10127. https://doi.org/10.5194/acp-24-10113-2024

Yang, Y., Liang, X. S., Qiu, B., and Chen, S. M. (2017). On the decadal variability of the eddy kinetic energy in the Kuroshio extension. *J. Phys. Oceanogr.*, *47*(5), 1169–1187. https://doi.org/10.1175/JPO-D-16-0201.1

Zeng, X. Y., and Zhong, G. (2024). Analysis of gravity wave activity during stratospheric sudden warmings in the northern hemisphere. *Earth Planet. Phys.*, *8*(2), 415–422. https://doi.org/10.26464/epp2024007

Zorkaltseva, O., Vasilyev, R. V., Mordvinov, V. I., and Dombrovskaya, N. S. (2019). Dynamics of the mesosphere and lower thermosphere during sudden stratospheric warmings over the Asian region. In *Proceedings Volume 11208, 25th International Symposium on Atmospheric and Ocean Optics: Atmospheric Physics* (pp. 1480–1484). Novosibirsk, Russian Federation: SPIE. https://doi.org/10.1117/12.2540077